RSC Advances

PAPER

View Article Online
View Journal | View Issue

Check for updates

Cite this: *RSC Adv.*, 2020, **10**, 22556

Highly spin-polarized electronic structure and magnetic properties of $Mn_{2.25}Co_{0.75}Al_{1-x}Ge_x$ Heusler alloys: first-principles calculations†

Yue Wang,[a] Liying Wang *[ab] and Wenbo Mi [a]

Received 16th April 2020
Accepted 4th June 2020

DOI: 10.1039/d0ra03413d

rsc.li/rsc-advances

Highly spin-polarized half-metals (HMs) and spin-gapless semiconductors (SGSs) are the promising candidates in spintronic devices. However, the HM and SGS Heusler materials are very sensitive to the stoichiometric defects and lattice distortion, which will be not beneficial to the practical applications. Here, the electronic structure and magnetic properties of $Mn_{2.25}Co_{0.75}Al_{1-x}Ge_x$ ($x = 0$, 0.25, 0.50, 0.75 and 1.00) Heusler alloys were investigated by first-principles calculations. Large negative formation energy, cohesive energy and phonon spectra confirm that the $Mn_{2.25}Co_{0.75}Al_{1-x}Ge_x$ alloys are stable. It is found that $Mn_{2.25}Co_{0.75}Al_{1-x}Ge_x$ with $x = 0$, 0.25, 0.75 and 1.00 show robust ferrimagnetic HM characteristics, while $Mn_{2.25}Co_{0.75}Al_{0.5}Ge_{0.5}$ shows robust SGS characteristic. Under the hydrostatic and uniaxial strains, $Mn_{2.25}Co_{0.75}Al_{1-x}Ge_x$ exhibit a series of rich electronic transitions. The magnetic anisotropy of $Mn_{2.25}Co_{0.75}Al_{1-x}Ge_x$ turns from the in-plane [100] direction to the out-of-plane [001] one by applying the uniaxial strains. The results suggest that the complete spin polarizations of $Mn_{2.25}Co_{0.75}Al_{1-x}Ge_x$ alloys are robust against the stoichiometric defects and lattice distortion, which have potential applications in spintronic devices.

1 Introduction

The half-metals (HMs)[1] and spin-gapless semiconductors (SGSs)[2] with high spin polarization have been paid much attention as the promising candidates in spintronic devices. HM was firstly predicted in NiMnSb by de Groot *et al.*,[3] where one spin channel is metallic and the other spin channel is semiconducting. Thus, HM can provide 100% spin polarized current. Up to now, HMs have been found in Heusler alloys,[4–7] diluted magnetic semiconductors,[8,9] perovskite compounds,[10,11] two dimensional materials,[12–14] zinc blende compounds,[15,16] nanowires,[17] nanoribbons[18,19] and nanotubes,[20] *etc.* SGS was firstly theoretically proposed and experimentally verified in Co-doped $PbPdO_2$,[21] where one spin channel is semiconducting and the other has an almost vanishing zero-width band gap at Fermi level. SGSs have been widely observed in Heusler alloys,[22–24] nanoribbons,[25] two-dimensional materials[26,27] and perovskite compounds,[28,29] *etc.* Both the electrons and holes in SGS and HM are 100% spin polarized, where no threshold energy needs to excite them from occupied states to empty ones. The special band structure of SGS leads to some unique properties, such as (i) high carrier mobility, (ii) tunable physical properties by external influences, (iii) the coexistence of high resistance and high Curie temperature, (iv) new spin injection source to overcome the conductivity mismatch. HM can provide the completely spin-polarized current, which is an ideal candidate in spintronic devices with high speed and low power consumption. Therefore, HMs and SGSs are attractive in spintronic devices, such as spin valves, spin diodes and spin filters.[30–32]

Heusler alloy is a remarkable class of intermetallic materials,[33] which has attracted much attention due to highly ordered atomic occupation and abundant atomic arrangement. The general formula of full Heusler alloy is the $L2_1$ ordered X_2YZ (Cu_2MnAl-type) with a space group of $Fm\bar{3}m$, like Co_2MnAl,[34] where X and Y are the transition metal elements, and Z are s–p elements. The full Heusler structure has four formula units per cubic unit cell with the atomic sequence X–Y–X–Z, two X occupy the Wyckoff-positions namely A (0, 0, 0) and C (1/2, 1/2, 1/2) sites, Y occupies B (1/4, 1/4, 1/4) sites and Z occupies D (3/4, 3/4, 3/4) sites, respectively. Generally, when X is less electronegative than Y, the atomic sequence changes to X–X–Y–Z[27,35] as Hg_2CuTi-type, which is also known as the inverse Heusler alloy with a space group of $F\bar{4}3m$, like Mn_2CoAl.[36,37] When one of the X atoms is removed, a $C1_b$-ordered half-Heusler structure XYZ (MgAgAs-type) with a space group of $F\bar{4}3m$ can be derived. Further, when one of X atoms is replaced by another transition

---

[a] Tianjin Key Laboratory of Low Dimensional Materials Physics and Preparation Technology, School of Science, Tianjin University, Tianjin 300354, China. E-mail: liying.wang@tju.edu.cn

[b] Tianjin Demonstration Center for Experimental Physics Education, School of Science, Tianjin University, Tianjin 300354, China

† Electronic supplementary information (ESI) available. See DOI: 10.1039/d0ra03413d

metal element M, a quaternary Heusler alloys X–M–Y–Z (LiMgPdSb-type) with a space group $F\bar{4}3m$ is obtained.

Lots of HMs and SGSs have been found in experiment and theory.[38–45] HMs and SGSs in Heusler alloys attract much attention due to the tunable electronic structures, high Curie temperature,[46–52] simple preparation procedure[53,54] and tunable magnetic anisotropy energy (MAE),[55,56] *etc.* However, the stoichiometric defect in Heusler alloys can destroy the HM and SGS characteristics, which usually happens during the preparation of bulk materials and thin films. Meanwhile, the HM and SGS characteristics can also be destroyed by lattice distortion due to the temperature or pressure changes.[57] Thus, the HMs and SGSs verified in experiments are much less than that predicted theoretically. Therefore, it is important to find the completely spin-polarized HM and SGS which are robust against the stoichiometric defects and lattice distortion. Additionally, the substitution is an effective way to tailor the electronic structure,[58–64] where the first SGS was obtained by substituting Co atom for Pd in $PbPdO_2$.[21,22] Ayuela *et al.* firstly reported that Co_2MnGa has a large spin-up density of states (DOS) at the Fermi level, while spin-down density of states at the Fermi level nearly vanishes, which results a high spin polarization despite it's not completely spin-polarized.[65] In the further exploration work, Varaprasad proved that the spin-polarization can be definitely increased in $Co_2MnGa_{0.5}Sn_{0.5}$ by substituting Sn atom for Ga in Co_2MnGa.[66] Feng *et al.* found that $Mn_2Co_{0.75}Cr_{0.25}Al$ can maintain the half-metallicity even though the lattice structure is disordered.[67] Li *et al.* found that the magnetic properties of Fe_4N can be tailored by doping rare-earth elements.[68]

Mn_2CoAl Heusler alloy has attracted great attention since its SGS behavior has been confirmed experimentally by Felser *et al.*[22] The complete spin polarization of SGS makes Mn_2CoAl a promising candidate in spintronic devices. However, the SGS characteristics of Mn_2CoAl were sensitive to the external strains, dopants and atomic disorder. Jamer *et al.* reported that the tetragonal distortion and atomic disorder which were introduced in epitaxial growth destroyed the SGS characteristics of Mn_2CoAl film on GaAs substrate.[69] It is necessary to address the issues of stoichiometry and chemical ordering of the sublattices. Galanakis *et al.* and Chen *et al.* pointed that the atomic swaps and Co-surplus during growth can destroy the SGS characteristics of Mn_2CoAl.[70,71] Mn_2CoGe is another HM with complete spin polarization.[37] It was reported that the high spin-polarized characteristics of Mn_2CoAl and Mn_2CoGe are robust and insensitive to Mn–Co disorder.[72] In this work, the electronic structure and magnetic properties of $Mn_{2.25}Co_{0.75}Al_{1-x}Ge_x$ (x = 0, 0.25, 0.50, 0.75 and 1.00) alloys are investigated by first-principles calculations. It is found that $Mn_{2.25}Co_{0.75}Al_{1-x}Ge_x$ alloys are stable, where the complete spin polarization is robust against the stoichiometric defects and lattice distortion. Meanwhile, the electronic structure and MAE of $Mn_{2.25}Co_{0.75}Al_{1-x}Ge_x$ can be tailored by applying hydrostatic and uniaxial strains. These results indicate that $Mn_{2.25}Co_{0.75}Al_{1-x}Ge_x$ alloys have the potential applications in spintronic devices for spin filter, high-density magnetic recording media *etc.*

2 Calculation details

The calculations are performed by Vienna *Ab initio* Simulation Package based on density functional theory.[73,74] The exchange correlation functional selects the Perdew–Burke–Ernzerhof[75] under generalized gradient approximation.[76] The projector augmented wave[77] method is used to describe the interaction between electrons and ions. The energy cutoff for plane-wave basis set is 500 eV. The valence electrons of Al, Mn, Co and Ge are $3s^23p^1$, $3d^64s^1$, $3d^84s^1$ and $4s^24p^2$, respectively. The Brillouin zone integration is performed using Monkhorst–Pack of 13 × 13 × 13. The convergence criteria of the energy and atomic force are set to 1×10^{-6} eV per atom and 1×10^{-3} eV $Å^{-1}$, respectively. Phonon spectrum is calculated by PHONOPY code[78] for $Mn_{2.25}Co_{0.75}Al_{1-x}Ge_x$ (x = 0, 0.25, 0.50, 0.75 and 1.00). Electronic structure and magnetic properties are calculated by considering the hydrostatic and uniaxial strains. The hydrostatic strain is defined as

$$\varepsilon_u = (a - a_0)/a_0 \times 100\%. \quad (1)$$

The uniaxial strain is defined as

$$\varepsilon_t = a/c \times 100\% \quad (2)$$

where a_0 is the lattice constant of the equilibrium unit cell, a and c are the lattice constants of the strained unit cell along [100] and [001] direction, respectively.

The MAE is obtained based on the magnetic force theorem method.[79] In order to get the reliable results, we have improved the accuracy of the MAE calculations with a much denser Monkhorst–Pack 32 × 32 × 32 k point meshes in the Brillouin zone.[80] Firstly, the accurate collinear calculation in the ground state is performed with 32 × 32 × 32 Monkhorst–Pack k point meshes. Then, the spin–orbital coupling is taken into account non-self-consistently to calculated the energy for [001] and [100] directions of the magnetic moment. Finally, MAE is calculated from the energy difference between the magnetic moment aligning along [001] and [100] directions,[81] which can be written as

$$\mathrm{MAE} = E_{[001]} - E_{[100]} \quad (3)$$

where $E_{[001]}$ and $E_{[100]}$ represent the total energy of the systems with magnetic moments along [001] and [100] magnetic direction, respectively. In order to obtain the orbital-resolved MAE, MAE on the orbital λ of atom i is defined as[68,82,83]

$$\mathrm{MAE}_{i\lambda} = E_{i\lambda}^{[001]} - E_{i\lambda}^{[100]} \quad (4)$$

where $E_{i\lambda}^{[001]}$ and $E_{i\lambda}^{[100]}$ represent the energy contribution from atom i and orbital λ as the magnetic moments aligning along [001] and [100] direction. The MAE of atom i is calculated by

$$\mathrm{MAE}_i = \sum_{\lambda} \mathrm{MAE}_{i\lambda} \quad (5)$$

The sum of MAE_i over all of the atoms in the same atomic layer is the layer-resolved MAE.

3 Results and discussion

3.1 Lattice structure

In inverse Heusler alloy Mn_2CoAl, Mn atoms occupy the Wyckoff-positions A (0, 0, 0) and B (1/4, 1/4, 1/4), which are labeled as Mn(A) and Mn(B), respectively. Co and Al atoms occupy C (1/2, 1/2, 1/2) and D (3/4, 3/4, 3/4), which are labeled as Co(C) and Al(D), respectively. So, the atomic sequence of Mn_2CoAl is Mn–Mn–Co–Al, as shown in Fig. 1(a). In order to construct $Mn_{2.25}Co_{0.75}Al_{1-x}Ge_x$ ($x = 0$, 0.25, 0.50, 0.75 and 1.00) alloys, Co and Al atoms in Mn_2CoAl are consecutively replaced by Mn and Ge. In a supercell with 4 formula units, 1 Co atom is substituted randomly by Mn and 0–4 Al atoms are substituted randomly by Ge. Fig. 1(b)–(f) show the atomic structure of $Mn_{2.25}Co_{0.75}Al_{1-x}Ge_x$ ($x = 0$, 0.25, 0.50, 0.75 and 1.00) alloys.

Fig. 1(g) shows the dependence of calculated total energy on lattice constant of Mn_2CoAl and $Mn_{2.25}Co_{0.75}Al_{1-x}Ge_x$ ($x = 0$, 0.25, 0.50, 0.75 and 1.00) alloys. The optimized equilibrium lattice constants are summarized in Table 1. In Fig. 1(g) and Table 1, the equilibrium lattice constant of Mn_2CoAl is 5.73 Å, which is consistent with the previous results.[84,85] The equilibrium lattice constants are 5.75 Å and 5.74 Å for $Mn_{2.25}Co_{0.75}Al_{1-x}Ge_x$ ($x = 0$ and 0.25) and $Mn_{2.25}Co_{0.75}Al_{1-x}Ge_x$ ($x = 0.50$, 0.75 and 1.00), respectively. The small variation of the equilibrium lattice constants can be ascribed to the similar atomic radius of Co and Mn atoms, as well as Al and Ge atoms.

3.2 Electronic structure and magnetic properties

Fig. 2 shows the spin-resolved band structure of Mn_2CoAl and $Mn_{2.25}Co_{0.75}Al_{1-x}Ge_x$ ($x = 0$, 0.25, 0.50, 0.75 and 1.00) alloys at the equilibrium lattice constant. It is found that the Mn_2CoAl and $Mn_{2.25}Co_{0.75}Al_{1-x}Ge_x$ ($x = 0$, 0.25, 0.50, 0.75 and 1.00) alloys show a semiconducting characteristic with a distinct energy gap in the spin-down channel (Fig. 2). The gap between the valence band maximum (VBM) and conduction band minimum (CBM) appears at G point of Brillouin zone (BZ), which is 0.384, 0.366, 0.308, 0.234, 0.201 and 0.238 eV for Mn_2CoAl and $Mn_{2.25}Co_{0.75}Al_{1-x}Ge_x$ ($x = 0$, 0.25, 0.50, 0.75 and 1.00), respectively. However, the spin-up band structure of $Mn_{2.25}Co_{0.75}Al_{1-x}Ge_x$ is different from Mn_2CoAl. In Mn_2CoAl, the VBM at G exactly touches the bottom of the CBM at X, which is a typical indirect zero-width gap at Fermi level in spin-up channel. So, Mn_2CoAl shows the SGS characteristics, which is in well agreement with the previous results.[22,85] In Fig. 2(d), the band structure of $Mn_{2.25}Co_{0.75}Al_{0.5}Ge_{0.5}$ shows the similar characteristics to Mn_2CoAl, which is also a SGS candidate at its ground state. However, in $Mn_{2.25}Co_{0.75}Al$, $Mn_{2.25}Co_{0.75}Al_{0.75}Ge_{0.25}$, $Mn_{2.25}Co_{0.75}Al_{0.25}Ge_{0.75}$ and $Mn_{2.25}Co_{0.75}Ge$, Ge substitution leads to continuous bands across E_F in spin-up channel, so all of them are HMs. Thus, the $Mn_{2.25}Co_{0.75}Al_{1-x}Ge_x$ ($x = 0$, 0.25, 0.50, 0.75 and 1.00) alloys are completely spin-polarized. A new kind of materials with complete spin polarization is predicted, which are robust against the stoichiometric defects.

Next, the effects of doped Mn and Ge on the band structure will be discussed in details. In Fig. 2(b), the partial Mn doping in $Mn_{2.25}Co_{0.75}Al$ creates a dense energy level around Fermi level and pushes the zero energy gap in spin-up channel to higher energy direction, resulting in a metallic characteristic in spin-up channel. So, the SGS characteristics disappear. However, the zero-width energy gap in the spin-up channel still exists in a higher energy region above E_F in $Mn_{2.25}Co_{0.75}Al$. It was expected that, with further doping of Ge, E_F should gradually shift towards to the conduction band edge. At $x = 0.5$, E_F exactly locates at the zero-width gap in $Mn_{2.25}Co_{0.75}Al_{0.5}Ge_{0.5}$, showing a SGS characteristic. With further Ge substitution, E_F continuously shifts to a higher energy. Finally, the energy gap shifts below E_F in $Mn_{2.25}Co_{0.75}Al_{0.25}Ge_{0.75}$ and $Mn_{2.25}Co_{0.75}Ge$, which results in the HM characteristics.

The total DOS of Mn_2CoAl and $Mn_{2.25}Co_{0.75}Al_{1-x}Ge_x$ ($x = 0$, 0.25, 0.50, 0.75 and 1.00) have been shown in Fig. 3. In Fig. 3, one can clearly see that the semiconducting band gaps appear in spin-down channels of the Mn_2CoAl and $Mn_{2.25}Co_{0.75}Al_{1-x}Ge_x$ ($x = 0$, 0.25, 0.50, 0.75 and 1.00) alloys. However, the spin-up electronic states go across Fermi level for all alloys, showing the HM characteristics with 100% spin polarization. In Mn_2CoAl

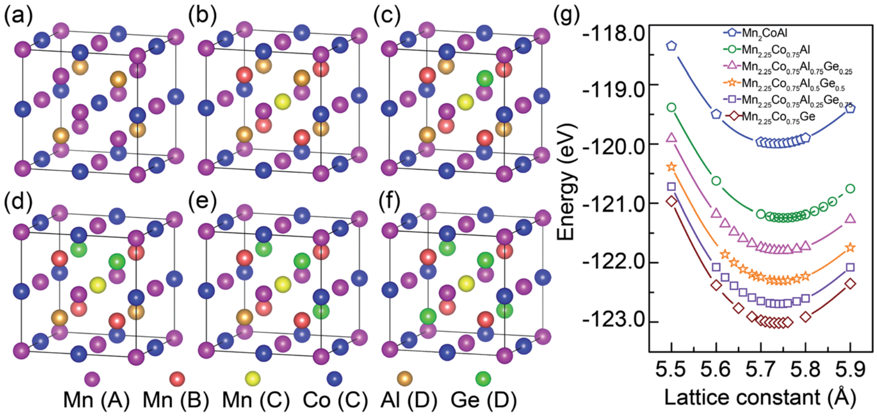

Fig. 1 Lattice structure of (a) Mn_2CoAl, (b) $Mn_{2.25}Co_{0.75}Al$, (c) $Mn_{2.25}Co_{0.75}Al_{0.75}Ge_{0.25}$, (d) $Mn_{2.25}Co_{0.75}Al_{0.5}Ge_{0.5}$, (e) $Mn_{2.25}Co_{0.75}Al_{0.25}Ge_{0.75}$ and (f) $Mn_{2.25}Co_{0.75}Ge$. (g) Lattice constant dependent total energy of Mn_2CoAl and $Mn_{2.25}Co_{0.75}Al_{1-x}Ge_x$ ($x = 0$, 0.25, 0.50, 0.75 and 1.00).

Table 1 Optimized equilibrium lattice constant a_0 (Å), total magnetic moment M_{tot} (μ_B per cell) and atomic magnetic moments M_z (μ_B per atom), formation energy E_{for} (eV) and cohesive energy E_{coh} (eV) of Mn$_2$CoAl and Mn$_{2.25}$Co$_{0.75}$Al$_{1-x}$Ge$_x$ (x = 0, 0.25, 0.50, 0.75 and 1.00)

Alloys	a_0	M_{tot}	$M_{Mn(A)}$	$M_{Mn(B)}$	$M_{Mn(C)}$	$M_{Co(C)}$	$M_{Al(D)}$	$M_{Ge(D)}$	E_{for}	E_{coh}
Mn$_2$CoAl	5.73	2.00	−1.54	2.63	—	0.95	−0.01	—	−1.59	−15.77
Mn$_{2.25}$Co$_{0.75}$Al	5.75	1.50	−1.59	2.67	−1.15	0.94	0	—	−1.44	−15.24
Mn$_{2.25}$Co$_{0.75}$Al$_{0.75}$Ge$_{0.25}$	5.75	1.75	−1.43	2.71	−0.93	0.93	0	0.03	−1.45	−14.01
Mn$_{2.25}$Co$_{0.75}$Al$_{0.5}$Ge$_{0.5}$	5.74	2.00	−1.23	2.73	−0.69	0.89	0	0.02	−1.44	−12.78
Mn$_{2.25}$Co$_{0.75}$Al$_{0.25}$Ge$_{0.75}$	5.74	2.25	−1.01	2.75	−0.59	0.88	0	0.02	−1.41	−11.51
Mn$_{2.25}$Co$_{0.75}$Ge	5.74	2.50	−0.82	2.78	−0.69	0.87	—	0.02	−1.36	−10.22

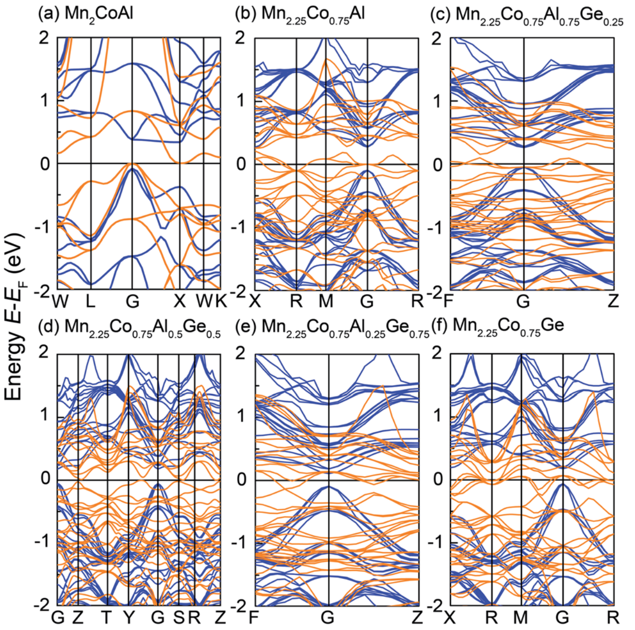

Fig. 2 Spin-resolved band structure of (a) Mn$_2$CoAl, (b) Mn$_{2.25}$Co$_{0.75}$Al, (c) Mn$_{2.25}$Co$_{0.75}$Al$_{0.75}$Ge$_{0.25}$, (d) Mn$_{2.25}$Co$_{0.75}$Al$_{0.5}$Ge$_{0.5}$, (e) Mn$_{2.25}$Co$_{0.75}$Al$_{0.25}$Ge$_{0.75}$ and (f) Mn$_{2.25}$Co$_{0.75}$Ge at equilibrium lattice constant. The orange and blue lines represent the spin-up and spin-down channels, respectively.

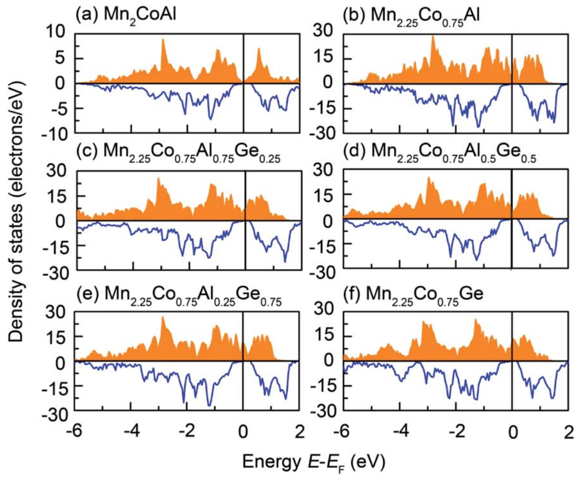

Fig. 3 Total DOS of (a) Mn$_2$CoAl, (b) Mn$_{2.25}$Co$_{0.75}$Al, (c) Mn$_{2.25}$Co$_{0.5}$Al$_{0.75}$G$_{0.25}$, (d) Mn$_{2.25}$Co$_{0.75}$Al$_{0.5}$Ge$_{0.5}$, (e) Mn$_{2.25}$Co$_{0.75}$Al$_{0.25}$Ge$_{0.75}$ and (f) Mn$_{2.25}$Co$_{0.75}$Ge. The positive and negative values represent the spin-up and spin-down channel, respectively.

and Mn$_{2.25}$Co$_{0.75}$Al$_{0.5}$Ge$_{0.5}$, E_F just falls into a zero-width energy gap, yielding a SGS nature. By comparing Fig. 3(a) with Fig. 3(b), it can be seen that the dense states appear around E_F in spin-up channel, which can attribute to the doped Mn. The slight E_F shift along the energy axis can be ascribed to the contribution of the doped Ge.

Fig. 4 shows the partial DOS of d components for Mn(A), Mn(B), Mn(C) and Co(C), as well as s/p states of Al(D) and Ge(D). It is found that a strong hybridization appears between the transition-metal atoms. In Fig. 3 and 4, three peaks occur in the spin-up channel. Two peaks of them locate in a lower energy region, which can be ascribed to the bonding states of Mn(B) and Co(C) sites. The peak at a higher energy region is mainly composed of the antibonding states of Mn(A) and Mn(C) atoms. In Mn$_{2.25}$Co$_{0.75}$Al$_{1-x}$Ge$_x$, two sharp peaks appear around Fermi level, where is a zero gap in Mn$_2$CoAl. These two peaks mainly come from the doped Mn(C) atom and move to a lower energy by doping Ge atoms. In the spin-down channel, the large band gap near E_F is kept for the Mn$_{2.25}$Co$_{0.75}$Al$_{1-x}$Ge$_x$ (x = 0, 0.25, 0.50, 0.75 and 1.00). A strong covalent hybridization happens between the d states of Mn(A), Mn(B), Mn(C) and Co(C) atoms, resulting in the formation of the bonding and antibonding bands separated by the gap. Similar to Mn$_2$CoAl, in the Mn$_{2.25}$Co$_{0.75}$Al$_{1-x}$Ge$_x$, the situations of Mn(A), Mn(C) and Co(C) atoms are different from Mn(B) atom. The partial DOS of Mn(A), Mn(C) and Co(C) have a similar gap width, while the Mn(B) atom has a larger gap width. Hence, the actual gap width in Mn$_{2.25}$Co$_{0.75}$Al$_{1-x}$Ge$_x$ alloys is mainly determined by Mn(A), Mn(C) and Co(C) atoms. The occupied bonding states at a lower energy region and unoccupied antibonding bands at 0.5–1.0 eV can be mainly attributed to Mn(A), Mn(C) and Co(C). The peak around 1.3 eV mainly arises from the antibonding nature of Mn(B) atom. Thus, the doped Mn(C) atom has a strong covalent hybridization with the other transition-metals in Mn$_{2.25}$Co$_{0.75}$Al$_{1-x}$Ge$_x$, which has an evident influence on the electronic states around E_F. Whereas, the doped Ge atoms mainly contribute more valence electrons in a lower energy region and push the E_F to a higher energy direction.

The total and atomic resolved magnetic moments of Mn$_2$CoAl and Mn$_{2.25}$Co$_{0.75}$Al$_{1-x}$Ge$_x$ (x = 0, 0.25, 0.50, 0.75 and 1.00) are listed in Table 1. The total magnetic moment of Mn$_2$CoAl and Mn$_{2.25}$Co$_{0.75}$Al$_{1-x}$Ge$_x$ (x = 0, 0.25, 0.50, 0.75 and 1.00) per unit formula is 2.00, 1.50, 1.75, 2.00, 2.25 and 2.50 μ_B,

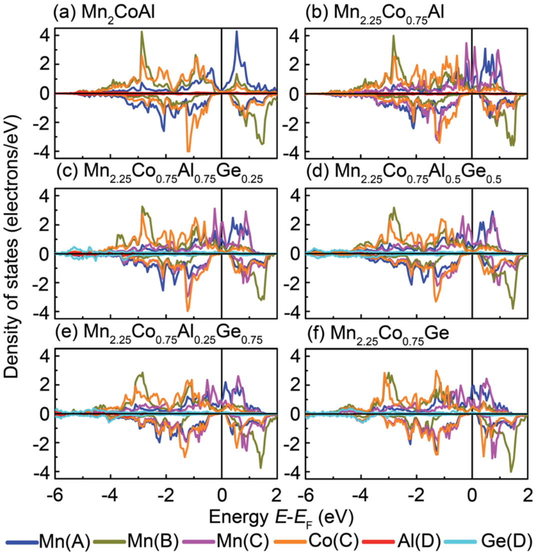

Fig. 4 Partial density of states (PDOS) of (a) Mn_2CoAl, (b) $Mn_{2.25}Co_{0.75}Al$, (c) $Mn_{2.25}Co_{0.75}Al_{0.75}Ge_{0.25}$, (d) $Mn_{2.25}Co_{0.75}Al_{0.5}Ge_{0.5}$, (e) $Mn_{2.25}Co_{0.75}Al_{0.25}Ge_{0.75}$ and (f) $Mn_{2.25}Co_{0.75}Ge$. The dark blue, brown, pink and orange lines represent the d orbitals of Mn(A), Mn(B), Mn(C) and Co(C) atoms, respectively. The red and light blue lines represent the s and p orbitals of Al and Ge, respectively. The positive and negative values represent the spin-up and spin-down channel, respectively.

respectively. The change of magnetic moments obeys the Slater-Pauling rule of $M_t = Z_t - 24$, where M_t is the total magnetic moment and Z_t is the number of valence electrons. Fig. 5 shows the variation of magnetic moments of Mn(A), Mn(B), Mn(C), Co(C) and total magnetic moments per formula unit of $Mn_{2.25}Co_{0.75}Al_{1-x}Ge_x$ at different x. In Fig. 5, it is found that the total magnetic moment of $Mn_{2.25}Co_{0.75}Al_{1-x}Ge_x$ almost increases linearly with Ge concentration, which can be ascribed to the decrease of the negative magnetic moments of Mn(A) and Mn(C) atoms. The magnetic moment of Mn(A) is antiparallel to that of Mn(B) and Co(C) atoms, but is parallel to Mn(C) atom. Mn(A) and Mn(C) atoms contribute the negative magnetic moments, while Mn(B) and Co(C) atoms contribute the positive values. Mn(B) is the main contributor to the total positive magnetic moments. At different Ge concentrations, the positive magnetic moments of Mn(B) and Co(C) almost remain unchanged. However, the negative moments of Mn(A) and Mn(C) decrease with the increase of Ge concentration. Combined with Table 1, it can be found that the variations of all the Mn and Co atomic magnetic moments are negligible when Al concentration was fixed as 100% (Mn_2CoAl and $Mn_{2.25}Co_{0.75}Al$). However, the substitution of nonmagnetic Ge atom affects the magnetic moments of Mn(A) and Mn(C) appreciably. As discussed in Fig. 3 and 4, the doped Ge atoms mainly contribute more valence electrons in a lower energy region, which leads to an increasement of the occupied states and pushes the E_F to the higher energy direction. From Fig. 4, it can be seen that there is a clearly unoccupied antibonding peak above the E_F in the spin-up channel for $Mn_{2.25}Co_{0.75}Al_{1-x}Ge_x$, which is mainly composed of the antibonding states of Mn(A) and Mn(C) atoms. Therefore, with the increasing Ge concentration in $Mn_{2.25}Co_{0.75}Al_{1-x}Ge_x$, the antibonding states of Mn(A) and Mn(C) move to lower energy region and the spin-splitting of Mn(A) and Mn(C) atoms will be reduced, which leads to the obviously reduction of Mn(A) and Mn(C) magnetic moments. In addition, the magnetic moments of Al and Ge atoms are comparatively negligible. So, Mn_2CoAl and $Mn_{2.25}Co_{0.75}Al_{1-x}Ge_x$ are ferrimagnetic HM/SGS materials with complete spin polarization.

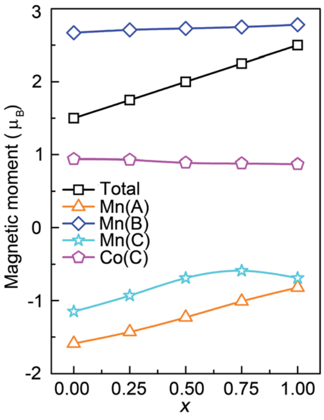

Fig. 5 Calculated total (per formula unit) and atomic magnetic moments of $Mn_{2.25}Co_{0.75}Al_{1-x}Ge_x$ at different x.

In order to investigate the effects of spin–orbit coupling (SOC), the electronic structure of Mn_2CoAl and $Mn_{2.25}Co_{0.75}Al_{1-x}Ge_x$ (x = 0, 0.25, 0.50, 0.75 and 1.00) is also calculated by considering SOC, as shown in Fig. S1.† It is found that SOC does not affect the HM/SGS characteristics of Mn_2CoAl and $Mn_{2.25}Co_{0.75}Al_{1-x}Ge_x$. Only some degenerated states are split into several singlet states at the high symmetry points. Thus, in the next sections (except for the MAE results), SOC also has not been considered.

Owing to the special band structures, the HM and SGS characteristics are sensitive to the stoichiometric defects, which usually happen during the preparation of Heusler bulk materials and thin films. Jamer *et al.* found that the atomic disorder which was introduced in epitaxial growth destroyed the SGS characteristics of Mn_2CoAl films.[69] Galanakis *et al.* and Chen *et al.* reported that Co-surplus and atomic swaps during growth also lead to the vanishing of the SGS characteristics in Mn_2CoAl.[70,71] Zhou *et al.* found that the substitution of Al by Si in Ti_2NiAl Heusler alloy destroyed its HM characteristics.[86] However, the present results clearly show that the $Mn_{2.25}Co_{0.75}Al_{1-x}Ge_x$ (x = 0, 0.25, 0.50, 0.75 and 1.00) alloys are new ferrimagnetic HM or SGS materials with 100% spin polarization, which is stable against the stoichiometric defects. The robust complete spin-polarization of $Mn_{2.25}Co_{0.75}Al_{1-x}Ge_x$ alloys makes them series promising candidates for the practical applications in spintronics devices.

3.3 Structure stability

It is necessary to check the structure stability of the alloys. Firstly, the formation energies (E_{for}) of Mn_2CoAl and

$Mn_{2.25}Co_{0.75}Al_{1-x}Ge_x$ ($x = 0$, 0.25, 0.50, 0.75 and 1.00) have been calculated based on the following formula

$$E_{\text{for}} = E^{\text{total}} - 2E_{\text{Mn}}^{\text{bulk}} - E_{\text{Co}}^{\text{bulk}} - E_{\text{Al}}^{\text{bulk}} \tag{6}$$

$$E_{\text{for}} = E^{\text{total}} - 2.25E_{\text{Mn}}^{\text{bulk}} - 0.75E_{\text{Co}}^{\text{bulk}} - (1-x)E_{\text{Al}}^{\text{bulk}} - xE_{\text{Ge}}^{\text{bulk}} \tag{7}$$

where E^{total} is the total energy of Mn_2CoAl and $Mn_{2.25}Co_{0.75}Al_{1-x}Ge_x$, $E_{\text{Mn}}^{\text{bulk}}$, $E_{\text{Co}}^{\text{bulk}}$, $E_{\text{Al}}^{\text{bulk}}$ and $E_{\text{Ge}}^{\text{bulk}}$ are the total energy of Mn, Co, Al and Ge, respectively. The calculated E_{for} of Mn_2CoAl and $Mn_{2.25}Co_{0.75}Al_{1-x}Ge_x$ ($x = 0$, 0.25, 0.50, 0.75 and 1.00) is −1.59, −1.44, −1.45, −1.44, −1.41 and −1.36 eV, respectively, as listed in Table 1. The negative formation energy indicates that Mn_2CoAl and $Mn_{2.25}Co_{0.75}Al_{1-x}Ge_x$ are expected to be stable. Then, the cohesive energy (E_{coh}) are calculated by

$$E_{\text{coh}} = E^{\text{total}} - 2E_{\text{Mn}}^{\text{iso}} - E_{\text{Co}}^{\text{iso}} - E_{\text{Al}}^{\text{iso}} \tag{8}$$

$$E_{\text{coh}} = E^{\text{total}} - 2.25E_{\text{Mn}}^{\text{iso}} - 0.75E_{\text{Co}}^{\text{iso}} - (1-x)E_{\text{Al}}^{\text{iso}} - xE_{\text{Ge}}^{\text{iso}} \tag{9}$$

where E^{total} are the total energy of Mn_2CoAl and $Mn_{2.25}Co_{0.75}Al_{1-x}Ge_x$. $E_{\text{Mn}}^{\text{iso}}$, $E_{\text{Co}}^{\text{iso}}$, $E_{\text{Al}}^{\text{iso}}$ and $E_{\text{Ge}}^{\text{iso}}$ are the isolated atomic energies of Mn, Co, Al and Ge, respectively. The cohesive energies of Mn_2CoAl and $Mn_{2.25}Co_{0.75}Al_{1-x}Ge_x$ ($x = 0$, 0.25, 0.50, 0.75 and 1.00) are −15.77, −15.24, −14.01, −12.78, −11.51 and −10.22 eV, respectively. The large negative cohesive energy indicates that the alloys are stable due to the high energy of the chemical bonds.

Furthermore, the phonon spectra of Mn_2CoAl and $Mn_{2.25}Co_{0.75}Al_{1-x}Ge_x$ at equilibrium lattice are shown in Fig. 6. Evidently, the spectra of all the alloys have no imaginary frequencies, which means that Mn_2CoAl and $Mn_{2.25}Co_{0.75}Al_{1-x}Ge_x$ ($x = 0$, 0.25, 0.50, 0.75 and 1.00) are dynamical stable. The structure stability indicates that Mn_2CoAl and $Mn_{2.25}Co_{0.75}Al_{1-x}Ge_x$ ($x = 0$, 0.25, 0.5, 0.75 and 1.00) may be realized in experiments. Fortunately, the Mn_2CoAl bulk and thin films have been successfully fabricated in experiments and proved to be SGS in previous reports.[67,68,83]

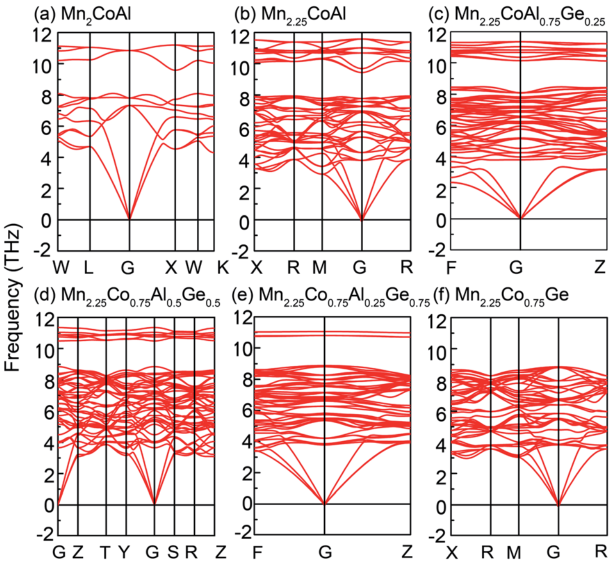

Fig. 6 Phonon spectrum of (a) Mn_2CoAl, (b) $Mn_{2.25}Co_{0.75}Al$, (c) $Mn_{2.25}Co_{0.75}Al_{0.75}Ge_{0.25}$, (d) $Mn_{2.25}Co_{0.75}Al_{0.5}Ge_{0.5}$, (e) $Mn_{2.25}Co_{0.75}Al_{0.25}Ge_{0.75}$ and (f) $Mn_{2.25}Co_{0.75}Ge$.

3.4 Effects of hydrostatic and uniaxial strains

It was known that the lattice deformation usually occurs during the film growth on different substrates. According to the previous theoretical and experimental results,[87] the electronic structure and magnetic properties of Heusler alloys are tunable under the hydrostatic (ε_u) and uniaxial (ε_t) strains. Owing to the varying of the lattice constant, the inter-atomic hybridization interaction and intra-atomic exchange interaction between transitional metal elements will be affected, which will influence the energy dispersion of the valence and conduction bands in the two spin directions. Here, the hydrostatic and uniaxial strains effects on Mn_2CoAl and $Mn_{2.25}Co_{0.75}Al_{1-x}Ge_x$ ($x = 0$, 0.25, 0.50, 0.75 and 1.00) are considered in the calculations. Fig. 7(a)–(i) show the location and width of the band gaps in spin-down channel of Mn_2CoAl and $Mn_{2.25}Co_{0.75}Al_{1-x}Ge_x$ ($x = 0$, 0.25, 0.50, 0.75 and 1.00) under hydrostatic and uniaxial strains, where the top of the bar represents the CBM location, the bottom of the bar represents the VBM location and the height of the bar indicates the bandwidth. In Fig. 7(a)–(f), the hydrostatic strain (ε_u) is considered from −6% to 6% in Mn_2CoAl and $Mn_{2.25}Co_{0.75}Al_{1-x}Ge_x$, where the positive and negative ε_u represent the tensile and compressive strains, respectively. In Fig. 7(a)–(f), the HM or SGS characteristics of Mn_2CoAl and $Mn_{2.25}Co_{0.75}Al_{1-x}Ge_x$ are quite robust against the varying ε_u. The half-metallic properties of $Mn_{2.25}Co_{0.75}Al_{1-x}Ge_x$ ($x = 0$, 0.25, 0.75 and 1.00) can be maintained in the ε_u range of −4–5%, −2–5%, −4–2% and −2–3%, respectively. The SGS properties of Mn_2CoAl and $Mn_{2.25}Co_{0.75}Al_{0.5}Ge_{0.5}$ can be kept in the ε_u range of −5–2% and −1–4%, respectively. The wide ε_u ranges where Mn_2CoAl and $Mn_{2.25}Co_{0.75}Al_{1-x}Ge_x$ can keep the HM and SGS characteristics indicate the robust stabilities of their HM and SGS properties. In Fig. 7(a)–(f), one can see that not only the gap width changes with the hydrostatic strains, but also the location of the gaps shift to lower or higher energy region. As a result, the rich electronic structure can be derived in Mn_2CoAl and $Mn_{2.25}Co_{0.75}Al_{1-x}Ge_x$ alloys. It should be noted that, for Mn_2CoAl, the spin direction of the conducting channel also changes with the hydrostatic strains. In Fig. 7(a), one can see that Mn_2CoAl undergoes HM with spin-up as conducting channel ($\varepsilon_u = -6\%$, as shown in Fig. 7(m)) → ferromagnetic semidoncuctor (FSC, $\varepsilon_u = -5\%$, as shown in Fig. 7(n)) → SGS with spin-down as conducting channel (in the ε_u range of −4–2%) → HM with spin-down as conducting channel (in the ε_u range of 3–6%) transitions with the varying hydrostatic strains, which is consistent with the previous result.[88] For $Mn_{2.25}Co_{0.75}Al_{1-x}Ge_x$ alloys, $Mn_{2.25}Co_{0.75}Al$ undergoes HM → general ferrimagnetic metal (GFM) → HM → GFM transitions (Fig. 7(b)). In Fig. 7(c), $Mn_{2.25}Co_{0.75}Al_{0.75}Ge_{0.25}$ undergoes GFM → HM → GFM transitions. In Fig. 7(d), $Mn_{2.25}Co_{0.75}Al_{0.5}Ge_{0.5}$ undergoes GFM → HM → SGS → GFM transitions. In Fig. 7(f), $Mn_{2.25}Co_{0.75}Ge$ undergoes HM → GFM → HM → GFM transitions. Particularly, $Mn_{2.25}Co_{0.75}Al_{0.25}Ge_{0.75}$ alloy can transfer

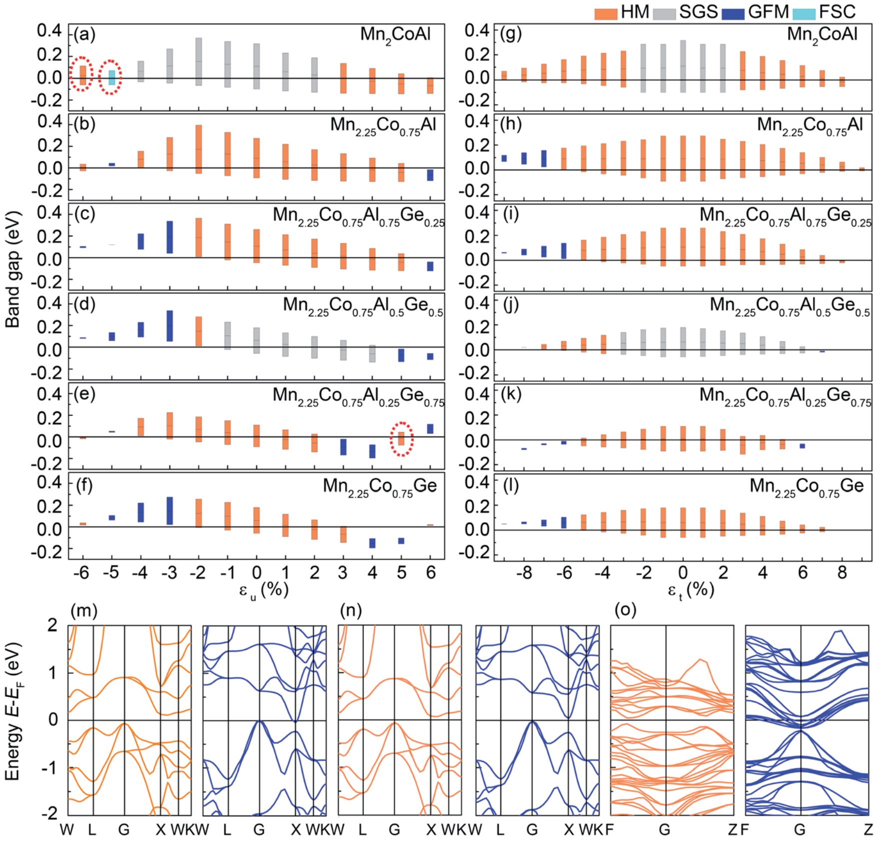

Fig. 7 Spin-dependent band gap, valence band maximum and conductance band minimum of Mn$_2$CoAl and Mn$_{2.25}$Co$_{0.75}$Al$_{1-x}$Ge$_x$ ($x = 0$, 0.25, 0.50, 0.75 and 1.00) under the (a)–(f) hydrostatic (ε_u) and (g)–(l) uniaxial (ε_t) strains. Fermi level is labeled by the horizontal lines. The orange, grey, and blue bars represent HM, SGS and general ferromagnetic metal, respectively. Spin-resolved band structure of (m) Mn$_2$CoAl at $\varepsilon_u = -6\%$, (n) Mn$_2$CoAl at $\varepsilon_u = -5\%$ and (o) Mn$_{2.25}$Co$_{0.75}$Al$_{0.25}$Ge$_{0.75}$ at $\varepsilon_u = 5\%$. The orange (blue) line represents spin-up (spin-down) channel.

from a HM to another HM with band gaps in opposite spin channels, which is similar to that of Mn$_2$CoAl. Namely, in Fig. 7(e), Mn$_{2.25}$Co$_{0.75}$Al$_{0.25}$Ge$_{0.75}$ undergoes HM with spin-up as conducting channel ($\varepsilon_u = -6\%$) → GFM ($\varepsilon_u = -5\%$) → HM with spin-up as conducting channel (in the ε_u range of −4–2%) → GFM (in the ε_u range of 3–4%) → HM with spin-down as conducting channel ($\varepsilon_u = 5\%$, as shown in Fig. 7(o)) → GFM ($\varepsilon_u = 6\%$) transitions, which can be derived from the different responses of the spin-up and spin-down electrons under strains. This rich electronic structures transition indicates that the spin polarization can be manipulated *via* applying external pressure and the polarized current direction of the spintronic devices may be inversed under extra influence, which will be good spintronics candidates used in pressure involved fields. The diverse and tunable electronic structures of Mn$_2$CoAl and Mn$_{2.25}$Co$_{0.75}$Al$_{1-x}$Ge$_x$ ($x = 0$, 0.25, 0.50, 0.75 and 1.00) make them quite promising to realize the relative spintronic applications in the future.

The effects of uniaxial strains (ε_t) on the electronic structure of Mn$_2$CoAl and Mn$_{2.25}$Co$_{0.75}$Al$_{1-x}$Ge$_x$ ($x = 0$, 0.25, 0.50, 0.75 and 1.00) are also investigated. In Fig. 7(g)–(l), the HM or SGS characteristics of Mn$_2$CoAl and Mn$_{2.25}$Co$_{0.75}$Al$_{1-x}$Ge$_x$ ($x = 0$, 0.25, 0.50, 0.75 and 1.00) are robust to the uniaxial strains. The HM properties of Mn$_{2.25}$Co$_{0.75}$Al$_{1-x}$Ge$_x$ ($x = 0$, 0.25, 0.75 and 1.00) can be preserved in the ε_t ranges of −6–9%, −5–8%, −5–5% and −5–7%, respectively. The SGS properties of Mn$_2$CoAl just can be kept in a relative narrow ε_t range of −2–2%, but it turns into HM at other ε_t. It has been found that the SGS characteristic of Mn$_2$CoAl films on GaAs was destroyed when a tetragonal distortion was introduced during the epitaxial growth.[68] However, the SGS characteristic of Mn$_{2.25}$Co$_{0.75}$Al$_{0.5}$Ge$_{0.5}$ can be kept in a wide ε_t range of −3–6%, which is better than Mn$_2$CoAl for practical applications. All of the alloys exhibit the electronic transitions under the uniaxial strains, as shown in Fig. 7(g)–(l). Namely, Mn$_2$CoAl undergoes the transition of HM → SGS → HM under the uniaxial strains, as shown in Fig. 7(g). Mn$_{2.25}$Co$_{0.75}$Al undergoes a GFM → HM transition, as shown in Fig. 7(h). Mn$_{2.25}$Co$_{0.75}$Al$_{0.75}$Ge$_{0.25}$ undergoes the GFM → HM transition as shown in Fig. 7(i). Mn$_{2.25}$Co$_{0.75}$Al$_{0.5}$Ge$_{0.5}$ undergoes the transition of HM → SGS → GFM (Fig. 7(j)). Mn$_{2.25}$Co$_{0.75}$Al$_{0.25}$Ge$_{0.75}$ undergoes the transition of GFM → HM → GFM (Fig. 7(k)). Mn$_{2.25}$Co$_{0.75}$Ge undergoes a GFM → HM transition (Fig. 7(l)). In Fig. 7(g)–(l), both the CBM and VBM shift towards Fermi level under the uniaxial strains, which results in the decrease of the bandwidth. The maximum bandwidth of Mn$_2$CoAl and Mn$_{2.25}$Co$_{0.75}$Al$_{1-x}$Ge$_x$ appears at the ground state ($\varepsilon_t = 0\%$).

The lattice deformation usually occurs during the film growth on different substrates, which may serve to destroy the HM and SGS properties. As reported by Jamer *et al.*, the SGS characteristics of Mn_2CoAl film on GaAs substrate were destroyed because the tetragonal distortion was introduced during epitaxial growth.[69] However, the HM and SGS characteristics of $Mn_{2.25}Co_{0.75}Al_{1-x}Ge_x$ ($x = 0$, 0.25, 0.50, 0.75 and 1.00) alloys are quite robust against the lattice distortions. Furthermore, the electronic structures of them can be tailored by the hydrostatic and uniaxial strains, which are beneficial to design the novel flexible spintronic devices.

3.5 Magnetic anisotropy

Ferromagnetic materials with the high magnetic anisotropy have attracted much attention for application in high-density magnetic recording media and nonvolatile magnetoresistive random access memory. The MAE of Mn_2CoAl and $Mn_{2.25}Co_{0.75}Al_{1-x}Ge_x$ ($x = 0$, 0.25, 0.50, 0.75 and 1.00) at the ground state is calculated. However, the calculated results show that the MAEs of all these alloys are nearly zero due to the cubic structure. Generally, the anisotropy of the ferromagnet is a combined effect of SOC and electrostatic crystal-field interactions. However, in cubic environments, cubic crystal-field states of 3d wave function are nearly quenched, which will lead to a zero MAE. Under the uniaxial strain, the cubic symmetry of Mn_2CoAl and $Mn_{2.25}Co_{0.75}Al_{1-x}Ge_x$ turns into the tetragonal symmetry, which can result in asymmetrical crystal field to enhance the magnetic anisotropy. Fig. 8 shows the MAEs of Mn_2CoAl and $Mn_{2.25}Co_{0.75}Al_{1-x}Ge_x$ at different uniaxial strains. Here, the negative MAE represents the magnetic easy axis along [001] direction (out of plane direction), and the positive one means the magnetic easy axis along [100] direction (in-plane direction). In Fig. 8, the similar trend appears in all the alloys at different uniaxial strains. By applying the uniaxial strain, the positive MAE turns into negative one, where MAE is positive at compressive strains and negative at tensile strains. Therefore, the magnetic anisotropy of the alloys can be tailored from in-plane direction to perpendicular one by applying the uniaxial strains. Meanwhile, the MAE value almost linearly increases with the increased compressive or tensile strain. $Mn_{2.25}Co_{0.75}Al_{0.25}Ge_{0.75}$ shows the biggest MAE at the uniaxial strain of −9% and 9%, which are 0.92 meV per unit cell and −0.88 meV per unit cell, respectively.

In order to further analyze the origin of the strain-dependent MAEs of $Mn_{2.25}Co_{0.75}Al_{1-x}Ge_x$, the layer and atom-resolved MAEs are calculated. Since the alloys show the similar MAE profiles (Fig. 8), only the layer and atom-resolved MAE of $Mn_{2.25}Co_{0.75}Al_{0.25}Ge_{0.75}$ is shown to discuss the MAE's origin, as shown in Fig. 9. The atom-resolved MAEs of Mn_2CoAl and $Mn_{2.25}Co_{0.75}Al_{1-x}Ge_x$ ($x = 0$, 0.25, 0.5, 1.00) have been shown in the ESI Fig. S2.† Owing to the element substitution and lattice distortion, the lattice symmetry is reduced, which results in different kinds of Mn(A), Mn(B) and Co(C) atoms, as shown in the inset of Fig. 9(a). The contribution of different Mn(A), Mn(B) and Co(C) atoms to MAE is different from each other. In Fig. 9(a), I/IV and II/III layers of the cubic $Mn_{2.25}Co_{0.75}Al_{0.25}Ge_{0.75}$ ($\varepsilon_t = 0\%$) exhibit a minor opposite MAE, which leads to a nearly zero MAE. The zero MAE mainly comes from the minor opposite MAE of Mn(A2) atom in I-layer and Mn(A3) atom in III-layer, as shown in Fig. 9(b). However, at $\varepsilon_t = -6\%$, MAE of each layer becomes positive, where the MAE of I- and III-layers significantly increases. The positive MAE can mainly be

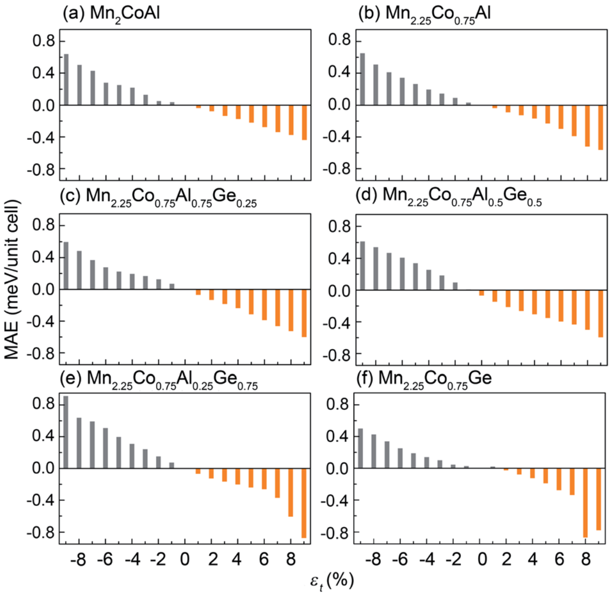

Fig. 8 MAE for (a) Mn_2CoAl, (b) $Mn_{2.25}Co_{0.75}Al$, (c) $Mn_{2.25}Co_{0.75}Al_{0.75}Ge_{0.25}$, (d) $Mn_{2.25}Co_{0.75}Al_{0.5}Ge_{0.5}$, (e) $Mn_{2.25}Co_{0.75}Al_{0.25}Ge_{0.75}$ and (f) $Mn_{2.25}Co_{0.75}Ge$ at different uniaxial strains.

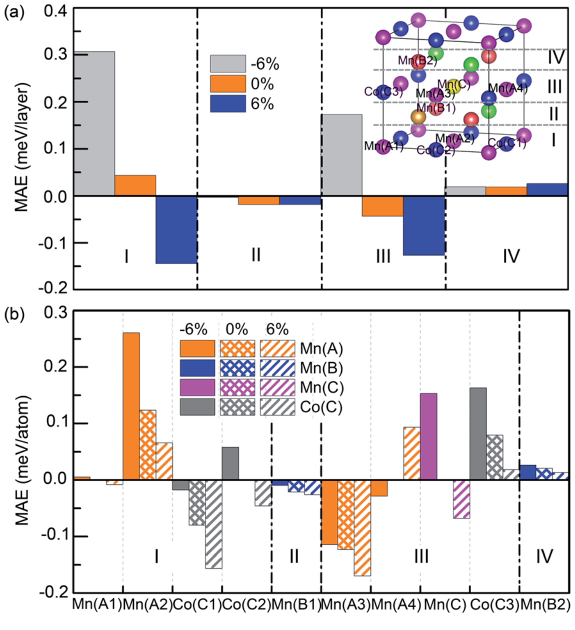

Fig. 9 (a) Layer- and (b) atomic-resolved MAE of $Mn_{2.25}Co_{0.75}Al_{0.25}Ge_{0.75}$ at a uniaxial strain of −6%, 0% and 6%. The inset of (a) shows the atomic structure of $Mn_{2.25}Co_{0.75}Al_{0.25}Ge_{0.75}$, where I–IV refers to the layer numbers.

attributed to Mn(A2) and Co(C2) atom in I-layer, Mn(C) and Co(C3) atoms in III-layer. Mn(A3) atom in III-layer contributes a relatively small negative MAE. So $Mn_{2.25}Co_{0.75}Si_{0.25}Ge_{0.75}$ exhibits the in-plane magnetic anisotropy at $\varepsilon_t = -6\%$. At $\varepsilon_t = 6\%$, every layer contributes a negative MAE, where Co(C1), Co(C2), Mn(A3), Mn(C) in I-, III-layers gives much contribution. Thus, the magnetic easy axis turns from the in-plane direction into the out-of-plane one.

Based on the second-order perturbation theory,[81,89] MAE can be defined as

$$\mathrm{MAE} \propto \xi^2 \sum_{\mathrm{o,u}} \frac{|\langle\psi_\mathrm{o}|\hat{L}_z|\psi_\mathrm{u}\rangle|^2 - |\langle\psi_\mathrm{o}|\hat{L}_x|\psi_\mathrm{u}\rangle|^2}{E_\mathrm{u} - E_\mathrm{o}} \tag{10}$$

where ψ_o and ψ_u indicate the occupied and unoccupied states with the energies E_o and E_u, respectively, $L\hat{}_z$ and $L\hat{}_x$ are the orbital angular momentum operators with the magnetization

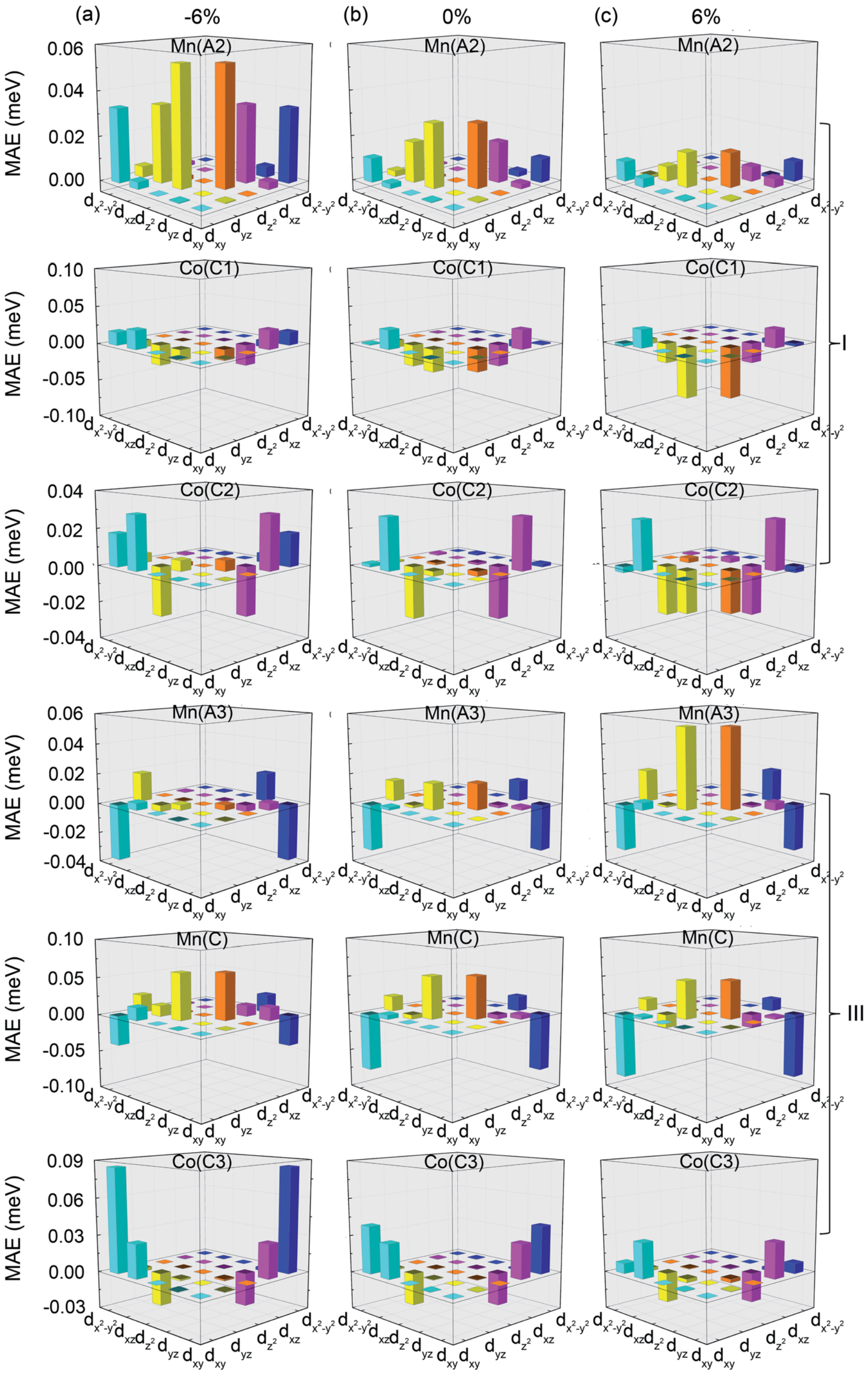

Fig. 10 Orbital-resolved MAE of Mn(A2), Co(C1), Co(C2) atoms in I-layer and Mn(A3), Mn(C), Co(C3) atoms in III-layer of $Mn_{2.25}Co_{0.75}Al_{0.25}Ge_{0.75}$ at (a) $\varepsilon_t = -6\%$, (b) $\varepsilon_t = 0\%$, and (c) $\varepsilon_t = 6\%$.

along [001] and [100] directions, ξ is the SOC constant. MAE depends on the nonzero coupling matrix element between the occupied and unoccupied states. The hybridizations between different orbitals can be used to analyze the origin of MAE. In order to further understand the origin of MAE of $Mn_{2.25}Co_{0.75}Al_{0.25}Ge_{0.75}$ at different uniaxial strains, the orbital-resolved MAE is calculated. As discussed above, the main source of MAE of $Mn_{2.25}Co_{0.75}Al_{0.25}Ge_{0.75}$ are the atoms in I- and III-layers. So, only the orbital-resolved MAE of the atoms in I- and III-layers is shown in Fig. 10. In the I-layer of $Mn_{2.25}Co_{0.75}Al_{0.25}Ge_{0.75}$, Mn(A2) contributes the significant positive MAE at $\varepsilon_t = -6\%$, which can be ascribed to the matrix element differences between the d_{xz} and d_{yz}, d_{xy} and $d_{x^2-y^2}$, as well as d_{z^2} and d_{yz} orbitals. Co(C1) d-orbitals only give a small contribution to the negative MAE and Co(C2) d-orbitals contribute a positive MAE. In III-layer, the Co(C3) contributions mainly come from the positive matrix element differences between the d_{xy} and $d_{x^2-y^2}$ orbitals. The positive MAE of Mn(C) can be attributed to the hybridized d_{z^2} and d_{yz} orbitals. Overall, only Mn(A3) gives a negative MAE, which mainly come from the hybridized d_{xy} and $d_{x^2-y^2}$ orbitals. Hence, at $\varepsilon_t = -6\%$, $Mn_{2.25}Co_{0.75}Al_{0.25}Ge_{0.75}$ shows the in-plane magnetic anisotropy, which can be mainly ascribed to the hybridized d-orbitals of Mn(A2), Co(C3) and Mn(C) atoms. At $\varepsilon_t = 6\%$, the in-plane component of Mn(A2) and Co(C3) d-orbitals decreases, whereas the out-of-plane component of Co(C1), Co(C2) and Mn(C) increase. The positive MAE of Mn(A3) which comes from the hybridized d_{z^2} and d_{yz} orbitals has a slight increasement. Overall, at $\varepsilon_t = 6\%$, $Mn_{2.25}Co_{0.75}Si_{0.25}Ge_{0.75}$ shows the perpendicular magnetic anisotropy. At $\varepsilon_t = 0\%$, the contribution of all the positive and negative MAE just exactly quenched to each other, as shown in Fig. 10(b). So, as ε_t changes from positive to negative, the magnetic anisotropy transits from the in-plane to the out-of-plane direction, which can be mainly attributed to the change of the d-orbitals hybridizations of Mn(A2)/Co(C1) in I-layer and Mn(C)/Co(C3) in III-layer.

The MAE results show that the magnetic anisotropy of the series $Mn_{2.25}Co_{0.75}Al_{1-x}Ge_x$ can be tailored from in-plane direction to perpendicular one under the uniaxial strains. Furthermore, the MAE values exhibit a linear dependence on uniaxial strains. It has been demonstrated experimentally that the easy axis of magnetization in the inverse spinels $CoFe_2O_4$ and $NiFe_2O_4$ can be tuned from perpendicular direction to in-plane one under tensile and compressive strains, respectively.[90,91] Thus, it may be an effective way to manipulate the magnetic anisotropy of $Mn_{2.25}Co_{0.75}Al_{1-x}Ge_x$ by applying uniaxial strain. In addition, all the PMA values of $Mn_{2.25}Co_{0.75}Al_{1-x}Ge_x$ can be up to more than -0.51 MJ m^{-3} (-0.6 meV per unit cell) at $\varepsilon_t = 9\%$ which is much larger than that of the reported Co-based Heusler films whose PMA values range from -0.09 MJ m^{-3} to -0.31 MJ m^{-3}.[55]

4 Conclusions

In summary, the electronic structure, stability and magnetic properties of $Mn_{2.25}Co_{0.75}Al_{1-x}Ge_x$ ($x = 0$, 0.25, 0.50, 0.75 and 1.00) are investigated by first-principles calculations. Our results reveal that the partial Mn doping in Mn_2CoAl creates a dense energy level around Fermi level and pushes the zero energy gap in Mn_2CoAl to higher energy direction, resulting in a metallic characteristic in $Mn_{2.25}Co_{0.75}Al$. The additional Ge atoms mainly contribute more valence electrons in a lower energy region and push the E_F to a higher energy direction, resulting in half-metallic behaviors for $Mn_{2.25}Co_{0.75}Al_{1-x}Ge_x$ with $x = 0$, 0.25, 0.75 and 1.00. However, at $x = 0.5$, E_F exactly locates at the zero energy gap in $Mn_{2.25}Co_{0.75}Al_{0.5}Ge_{0.5}$, showing a SGS characteristic again. The series of the $Mn_{2.25}Co_{0.75}Al_{1-x}Ge_x$ are confirmed that they are promising to be fabricated in experiment based on the stability calculational results. The HM or SGS characteristics of $Mn_{2.25}Co_{0.75}Al_{1-x}Ge_x$ can be kept in wide ranges of hydrostatic and uniaxial strains. For example, the SGS characteristics of $Mn_{2.25}Co_{0.75}Al_{0.5}Ge_{0.5}$ can be kept in the wide ε_u and ε_t range of −1–4% and −3–6%, respectively, which is even better than that of Mn_2CoAl for practical applications. The magnetic anisotropy energy of Mn_2CoAl and $Mn_{2.25}Co_{0.75}Al_{1-x}Ge_x$ are nearly zero due to the cubic structure. However, we show that the magnetic anisotropy energy in these alloys almost linearly improves with varying uniaxial strains, while showing an opposite response to compressive and tensile strain. As a result, the magnetic anisotropy of Mn_2CoAl and $Mn_{2.25}Co_{0.75}Al_{1-x}Ge_x$ can be manipulated from the in-plane [100] direction to the out-of-plane [001] one under uniaxial strains. The results suggest that $Mn_{2.25}Co_{0.75}Al_{1-x}Ge_x$ alloys are very promising for spintronics applications such as spin injection and spin valves.

Conflicts of interest

There are no conflicts to declare.

Acknowledgements

This work was supported by National Nature Science Foundations of China (Grant No. 51701138) and Natural Science Foundation of Tianjin City (Grant No. 17JCQNJC02800, 16JCYBJC17200).

Notes and references

1 C. Lidig, J. Minár, J. Braun, H. Ebert, A. Gloskovskii, J. A. Krieger, V. Strocov, M. Kläui and M. Jourdan, Surface resonance of thin films of the Heusler half-metal Co_2MnSi probed by soft X-ray angular resolved photoemission spectroscopy, *Phys. Rev. B*, 2019, **99**(17), 174432.

2 X. L. Wang, Dirac spin-gapless semiconductors: promising platforms for massless and dissipationless spintronics and new (quantum) anomalous spin Hall effects, *Natl. Sci. Rev.*, 2017, **4**(2), 252–257.

3 R. A. de Groot, F. M. Mueller, P. G. van Engen and K. H. J. Buschow, New class of materials: half-metallic ferromagnets, *Phys. Rev. Lett.*, 1983, **50**(25), 2024–2027.

4 M. Moradi, N. Taheri and M. Rostami, Structural, electronic, magnetic and vibrational properties of half-Heusler NaZrZ (Z = P, As, Sb) compounds discussion, *Phys. Lett. A*, 2018, **382**(41), 3004–3011.

5 M. Ram, A. Saxena, A. E. Aly and A. Shankar, Half-metallicity in new Heusler alloys Mn_2ScZ (Z = Si, Ge, Sn), *RSC Adv.*, 2020, **10**(13), 7661–7670.

6 L. Fan, F. Chen and Z. Q. Chen, First-principles calculations of magnetism and half-metallic properties of $CsYO_2$ (Y = V, Cr, Mn, Fe, Co, Ni) Heusler alloys, *J. Magn. Magn. Mater.*, 2019, **478**, 264–273.

7 S. Bahramian and F. Ahmadian, Half-metallicity and magnetism of quaternary Heusler compounds CoRuTiZ (Z = Si, Ge, and Sn), *J. Magn. Magn. Mater.*, 2017, **424**, 122–129.

8 W. Y. Yu, Z. L. Zhu, C. Y. Niu, C. Li, J. H. Cho and Y. Jia, Dilute magnetic semiconductor and half-metal behaviors in 3d transition-metal doped black and blue phosphorenes: a first-principles study, *Nanoscale Res. Lett.*, 2016, **11**, 1–9.

9 F. Ahmadian, Electronic and magnetic properties of diluted magnetic semiconductors $Zn_{1-x}V_xSe$ in zincblende structure, *Solid State Commun.*, 2011, **151**(21), 1622–1626.

10 N. N. Zu, R. Li, Q. N. Li and J. Wang, Electronic and magnetic properties of Sr_2MoBO_6 (B = W, Re, Os): investigation of possible half metal, *J. Magn. Magn. Mater.*, 2016, **399**, 72–76.

11 L. Ding, D. D. Khalyavin, P. Manuel, J. Blake, F. Orlandi, W. Yi and A. A. Belik, Colossal magnetoresistance in the insulating ferromagnetic double perovskites Tl_2NiMnO_6: a neutron diffraction study, *Acta Mater.*, 2019, **173**, 20–26.

12 J. Y. Liu, Z. F. Liu, T. L. Song and X. Cui, Computational search for two-dimensional intrinsic half-metals in transition-metal dinitrides, *J. Mater. Chem. C*, 2017, **5**(3), 727–732.

13 F. Aguilera-Granja and A. Ayuela, Magnetism and distortions in two-dimensional transition-metal dioxides: on the quest for intrinsic magnetic semiconductor layers, *J. Phys. Chem. C*, 2020, **124**(4), 2634–2643.

14 J. M. Zheng, R. J. He, Y. Wan, P. J. Zhao, P. Guo and Z. Y. Jiang, Half-metal state of a Ti_2C monolayer by asymmetric surface decoration, *Phys. Chem. Chem. Phys.*, 2019, **21**(6), 3318–3326.

15 J. E. Pask, L. H. Yang, C. Y. Fong, W. E. Pickett and S. Dag, Six low-strain zinc-blende half metals: an *ab initio* investigation, *Phys. Rev. B: Condens. Matter Mater. Phys.*, 2003, **67**(22), 224420.

16 M. Moradi, M. Rostami and M. Afshari, Half-metallic ferromagnetism in wurtzite and rocksalt TiTe: a density functional theory study, *Comput. Mater. Sci.*, 2013, **69**, 278–283.

17 P. Lou and J. Y. Lee, Singular nonmagnetic semiconductor SCH_3 molecular nanowire: a new type of room-temperature spintronic material, *J. Phys. Chem. C*, 2019, **123**(27), 16994–17001.

18 Y. W. Son, M. L. Cohen and S. G. Louie, Half-metallic graphene nanoribbons, *Nature*, 2006, **444**(7117), 347–349.

19 S. C. Zhu, C. T. Yip, S. J. Peng, K. M. Wu, K. L. Yao, C. L. Mak and C. H. Lam, Half-metallic and magnetic semiconducting behaviors of metal-doped blue phosphorus nanoribbons from first-principles calculations, *Phys. Chem. Chem. Phys.*, 2018, **20**(11), 7635–7642.

20 K. W. Lee and C. E. Lee, Half-Metallic Carbon Nanotubes, *Adv. Mater.*, 2012, **24**(15), 2019–2023.

21 X. L. Wang, Proposal for a new class of materials: spin gapless semiconductors, *Phys. Rev. Lett.*, 2008, **100**(15), 156404.

22 S. Ouardi, G. H. Fecher and C. Felser, Realization of spin gapless semiconductors: the Heusler compound Mn_2CoAl, *Phys. Rev. Lett.*, 2013, **110**(10), 100401.

23 G. Y. Gao and K. L. Yao, Antiferromagnetic half-metals, gapless half-metals, and spin gapless semiconductors: The $D0_3$-type Heusler alloys, *Appl. Phys. Lett.*, 2013, **103**(23), 232409.

24 X. T. Wang, Z. X. Cheng, J. L. Wang, X. L. Wang and G. D. Liu, Recent advances in the Heusler based spin-gapless semiconductors, *J. Mater. Chem. C*, 2016, **4**(30), 7176–7192.

25 Y. Ding and Y. L. Wang, Electronic structures of zigzag silicene nanoribbons with asymmetric sp^2–sp^3 edges, *Appl. Phys. Lett.*, 2013, **102**(14), 143115.

26 J. Lei, M. C. Xu and S. J. Hu, Anchoring transition metal elements on graphene-like ZnO monolayer by CO molecule to obtain spin gapless semiconductor, *Appl. Surf. Sci.*, 2017, **416**, 681–685.

27 A. Z. Wang, X. M. Zhang, Y. P. Feng and M. W. Zhao, Chern insulator and Chern half-metal states in the two-dimensional spin-gapless semiconductor $Mn_2C_6S_{12}$, *J. Phys. Chem. Lett.*, 2017, **8**(16), 3770–3775.

28 H. M. Huang, Z. Y. Jiang, Y. M. Lin, B. Z. Zhou and C. K. Zhang, Design of half-metal and spin gapless semiconductor for spintronics application *via* cation substitution in methylammonium lead iodide, *Appl. Phys. Express*, 2017, **10**(12), 123002.

29 H. P. Wu, Y. Qian, W. S. Tan, E. J. Kan, R. F. Lu and K. M. Deng, Vacancy-induced insulator-direct spin gapless semiconductor-half-metal transition in double perovskite La_2CrFeO_6: a first-principles study, *Phys. Lett. A*, 2015, **379**(43–44), 2897–2901.

30 V. Varade, T. Markus, K. Vankayala, N. Friedman, M. Sheves, D. H. Waldeck and R. Naaman, Bacteriorhodopsin based non-magnetic spin filters for biomolecular spintronics, *Phys. Chem. Chem. Phys.*, 2018, **20**(2), 1091–1097.

31 Z. H. Xiong, D. Wu, Z. V. Vardeny and J. Shi, Giant magnetoresistance in organic spin-valves, *Nature*, 2004, **427**(6977), 821–824.

32 F. J. Jedema, M. S. Nijboer, A. T. Filip and B. J. van Wees, Spin injection and spin accumulation in all-metal mesoscopic spin valves, *Phys. Rev. B: Condens. Matter Mater. Phys.*, 2003, **67**(8), 085319.

33 F. Heusler, W. Starck and E. Haupt, Magnetisch-chemische studien, *Verh. Dtsch. Phys. Ges.*, 1903, **5**, 219–232.

34 I. Di Marco, A. Held, S. Keshavarz, Y. O. Kvashnin and L. Chioncel, Half-metallicity and magnetism in the

Co_2MnAl/CoMnVAl heterostructure, *Phys. Rev. B*, 2018, **97**(3), 035105.

35 I. Galanakis, P. Mavropoulos and P. H. Dederichs, Electronic structure and Slater-Pauling behaviour in half-metallic Heusler alloys calculated from first principles, *J. Phys. D: Appl. Phys.*, 2006, **39**(5), 765–775.

36 H. Z. Luo, H. W. Zhang, Z. Y. Zhu, L. Ma, S. F. Xu, G. H. Wu, X. X. Zhu, C. B. Jiang and H. B. Xu, Half-metallic properties for the Mn_2FeZ (Z = Al, Ga, Si, Ge, Sb) Heusler alloys: a first-principles study, *J. Appl. Phys.*, 2008, **103**(8), 083908.

37 G. D. Liu, X. F. Dai, H. Y. Liu, J. L. Chen, Y. X. Li, G. Xiao and G. H. Wu, Mn_2CoZ (Z = Al, Ga, In, Si, Ge, Sn, Sb) compounds: structural, electronic, and magnetic properties, *Phys. Rev. B: Condens. Matter Mater. Phys.*, 2008, **77**(1), 014424.

38 P. Wang, J. B. Xia and H. B. Wu, Electronic structures, magnetic properties and strain effects of quaternary Heusler alloys FeMnCrZ (Z = P, As, Sb, Bi, Se, Te), *J. Magn. Magn. Mater.*, 2019, **490**, 165490.

39 S. A. Khandy and J. D. Chai, Novel half-metallic $L2_1$ structured full-Heusler compound for promising spintronic applications: a DFT-based computer simulation, *J. Magn. Magn. Mater.*, 2019, **487**, 165289.

40 L. Fan, F. Chen and Z. Q. Chen, First-principles calculations of magnetism and half-metallic properties of $CsYO_2$ (Y = V, Cr, Mn, Fe, Co, Ni) Heusler alloys, *J. Magn. Magn. Mater.*, 2019, **478**, 264–273.

41 M. Baral and A. Chakrabarti, Half-metallicity *versus* symmetry in half-Heusler alloys based on Pt, Ni, and Co: an *ab initio* study, *Phys. Rev. B*, 2019, **99**(20), 205136.

42 L. Fan, F. Chen, C. M. Li, X. Hou, X. Zhu, J. L. Luo and Z. Q. Chen, Promising spintronics: Mn-based Heusler alloys Mn_3Ga, Mn_2YGa (Y = V, Nb, Ta), ScMnVGa, *J. Magn. Magn. Mater.*, 2020, **497**, 166060.

43 M. I. Khan, H. Arshad, M. Rizwan, S. S. A. Gillani, M. Zafar, S. Ahmed and M. Shakil, Investigation of structural, electronic, magnetic and mechanical properties of a new series of equiatomic quaternary Heusler alloys CoYCrZ (Z = Si, Ge, Ga, Al): a DFT study, *J. Alloys Compd.*, 2019, **819**, 152964.

44 G. Z. Xu, Y. Du, X. M. Zhang, H. G. Zhang, E. K. Liu, W. H. Wang and G. H. Wu, Magneto-transport properties of oriented Mn_2CoAl films sputtered on thermally oxidized Si substrates, *Appl. Phys. Lett.*, 2014, **104**(24), 242408.

45 P. Chen, C. X. Gao, G. L. Chen, K. Mi, M. Liu, P. Zhang and D. S. Xue, The low-temperature transport properties of Heusler alloy Mn_2CoAl, *Appl. Phys. Lett.*, 2018, **113**(12), 122402.

46 S. Picozzi, A. Continenza and A. J. Freeman, Co_2MnX (X = Si, Ge, Sn) Heusler compounds: an *ab initio* study of their structural, electronic, and magnetic properties at zero and elevated pressure, *Phys. Rev. B: Condens. Matter Mater. Phys.*, 2002, **66**(9), 094421.

47 S. Ishida, S. Fujii, S. Kashiwagi and S. Asano, Search for half-metallic compounds in Co_2MnZ (Z = IIIb, IVb, Vb element), *J. Phys. Soc. Jpn.*, 1995, **64**(6), 2152–2157.

48 I. Galanakis, P. H. Dederichs and N. Papanikolaou, Slater-Pauling behavior and origin of the half-metallicity of the full-Heusler alloys, *Phys. Rev. B: Condens. Matter Mater. Phys.*, 2002, **66**(17), 174429.

49 M. Yamamoto, T. Ishikawa, T. Taira, G. Li, K. Matsuda and T. Uemura, Effect of defects in Heusler alloy thin films on spin-dependent tunnelling characteristics of Co_2MnSi/MgO/Co_2MnSi and Co_2MnGe/MgO/Co_2MnGe magnetic tunnel junctions, *J. Phys.: Condens. Matter*, 2010, **22**(16), 164212.

50 S. Tsunegi, Y. Sakuraba, M. Oogane, K. Takanashi and Y. Ando, Large tunnel magnetoresistance in magnetic tunnel junctions using a Co_2MnSi Heusler alloy electrode and a MgO barrier, *Appl. Phys. Lett.*, 2008, **93**(11), 112506.

51 T. Ishikawa, T. Marukame, H. Kijima, K.-I. Matsuda, T. Uemura, M. Arita and M. Yamamoto, Spin-dependent tunneling characteristics of fully epitaxial magnetic tunneling junctions with a full-Heusler alloy Co_2MnSi thin film and a MgO tunnel barrier, *Appl. Phys. Lett.*, 2006, **89**(19), 192505.

52 X. H. Zhu, E. H. Jiang, Y. F. Dai and C. L. Luo, Stability, magnetic, and electronic properties of $L2_1$ and B2 phases in Co_2MnAl Heusler alloy, *J. Alloys Compd.*, 2015, **632**, 528–532.

53 L. Bainsla, A. I. Mallick, M. M. Raja, A. K. Nigam, B. S. D. C. S. Varaprasad, Y. K. Takahashi, A. Alam, K. G. Suresh and K. Hono, Spin gapless semiconducting behavior in equiatomic quaternary CoFeMnSi Heusler alloy, *Phys. Rev. B: Condens. Matter Mater. Phys.*, 2015, **91**(10), 104408.

54 M. E. Jamer, B. A. Assaf, G. E. Sterbinsky, D. Arena, L. H. Lewis, A. A. Saúl, G. Radtke and D. Heiman, Antiferromagnetic phase of the gapless semiconductor V_3Al, *Phys. Rev. B: Condens. Matter Mater. Phys.*, 2015, **91**(9), 094409.

55 Y. Wu, X. G. Xu, J. Miao and Y. Jiang, Perpendicular magnetic anisotropy in Co-based full heusler alloy thin films, *Spin*, 2015, **5**(4), 1540012.

56 W. H. Wang, M. Przybylski, W. Kuch, L. I. Chelaru, J. Wang, Y. F. Lu, J. Barthel, H. L. Meyerheim and J. Kirschner, Magnetic properties and spin polarization of Co_2MnSi Heusler alloy thin films epitaxially grown on GaAs(001), *Phys. Rev. B: Condens. Matter Mater. Phys.*, 2005, **71**(14), 144416.

57 G. Y. Gao, G. Q. Ding, J. Li, K. L. Yao, M. H. Wu and M. C. Qian, Monolayer MXenes: promising half-metals and spin gapless semiconductors, *Nanoscale*, 2016, **8**(16), 8986–8994.

58 H. Z. Luo, F. B. Meng, Z. Q. Feng, Y. X. Li, W. Zhu, G. H. Wu, X. X. Zhu, C. B. Jiang and H. B. Xu, The structural and magnetic properties of $Mn_{2-x}Fe_xNiGa$ Heusler alloys, *J. Appl. Phys.*, 2010, **107**(1), 013905.

59 M. Meinert, J. M. Schmalhorst, G. Reiss and E. Arenholz, Ferrimagnetism and disorder of epitaxial $Mn_{2-x}Co_xVAl$ Heusler compound thin films, *J. Phys. D: Appl. Phys.*, 2011, **44**(21), 215003.

60 M. Y. Jiang, M. G. Samant, C. Felser and S. S. P. Parkin, Strong dependence of the tetragonal $Mn_{2.1}Ga$ thin film

crystallization temperature window on seed layer, *Appl. Phys. Lett.*, 2013, **103**(3), 032410.

61 Z. W. Du, X. L. Han, T. Li, E. K. Liu, X. D. Ma, J. C. Xiong and G. H. Wu, Microstructures and phase transformations in as-aged $Mn_{2.04}NiGa$ Heusler alloy, *J. Alloys Compd.*, 2016, **657**, 443–449.

62 R. Gavrea, C. Leostean, M. Coldea, O. Isnard, V. Pop and D. Benea, Effects of Co for Mn substitution on the electronic properties of $Mn_{2-x}Co_xVAl$ as probed by XPS, *Intermetallics*, 2018, **93**, 155–161.

63 A. Kalache, A. Markou, S. Selle, T. Höche, R. Sahoo, G. H. Fecher and C. Felser, Heteroepitaxial growth of tetragonal $Mn_{2.7-x}Fe_xGa_{1.3}$ ($0 \leq x \leq 1.2$) Heusler films with perpendicular magnetic anisotropy, *APL Mater.*, 2017, **5**, 096102.

64 M. Ram, A. Saxena, A. E. Aly and A. Shankar, Study of half metallicity, structural and mechanical properties in inverse Heusler alloy $Mn_2ZnSi_{(1-x)}Ge_x$ and a superlattice, *RSC Adv.*, 2019, **9**(63), 36680–36689.

65 A. Ayuela, J. Enkovaara, K. Ullakko and R. M. Nieminen, Structural properties of magnetic Heusler alloys, *J. Phys.: Condens. Matter*, 1999, **11**, 2017–2026.

66 B. S. D. C. S. Varaprasad, A. Srinivasan, Y. K. Takahashi and K. Hono, Highly spin-polarized $Co_2MnGa_{0.5}Sn_{0.5}$ Heusler compound, *Acta Mater.*, 2009, **57**(9), 2702–2709.

67 X. Feng, L. Feng, C. C. Guo and W. X. Zhang, First-principles investigation of half-metallicity of $Mn_2Co_{1-x}Cr_xAl$, *Comput. Mater. Sci.*, 2017, **127**, 15–21.

68 Z. R. Li, W. B. Mi and H. L. Bai, The role of rare-earth dopants in tailoring the magnetism and magnetic anisotropy in Fe_4N, *J. Phys. Chem. Solids*, 2018, **116**, 7–14.

69 M. E. Jamer, B. A. Assaf, T. Devakul and D. Heiman, Magnetic and transport properties of Mn_2CoAl oriented films, *Appl. Phys. Lett.*, 2013, **103**(14), 142403.

70 I. Galanakis, K. Özdoğan, E. Şaşıoğlu and S. Blügel, Conditions for spin-gapless semiconducting behavior in Mn_2CoAl inverse Heusler compound, *J. Appl. Phys.*, 2014, **115**(9), 093908.

71 X. R. Chen, M. M. Zhong, Y. Feng, Y. Zhou, H. K. Yuan and H. Chen, Structural, electronic, elastic, and thermodynamic properties of the spin-gapless semiconducting Mn_2CoAl inverse Heusler alloy under pressure, *Phys. Status Solidi B*, 2015, **252**(12), 2830–2839.

72 Y. P. Xin, H. Y. Hao, Y. X. Ma, H. Z. Luo, F. B. Meng, H. Y. Liu, E. K. Liu and G. H. Wu, Competition of XA and $L2_1B$ ordering in Heusler alloys Mn_2CoZ (Z = Al, Ga, Si, Ge and Sb) and its influence on electronic structure, *Intermetallics*, 2017, **80**, 10–15.

73 G. Kresse and J. Furthmüller, Efficiency of *ab initio* total energy calculations for metals and semiconductors using a plane-wave basis set, *Comput. Mater. Sci.*, 1996, **6**(1), 15–50.

74 G. Kresse and J. Furthmüller, Efficient iterative schemes for *ab initio* total-energy calculations using a plane-wave basis set, *Phys. Rev. B: Condens. Matter Mater. Phys.*, 1996, **54**(16), 11169–11186.

75 D. Vanderbilt, Soft self-consistent pseudopotentials in a generalized eigenvalue formalism, *Phys. Rev. B: Condens. Matter Mater. Phys.*, 1990, **41**, 7892–7895.

76 M. Marlo and V. Milman, Density-functional study of bulk and surface properties of titanium nitride using different exchange-correlation functional, *Phys. Rev. B: Condens. Matter Mater. Phys.*, 2000, **62**(4), 2899–2907.

77 X. Blanc, É. Cancès and M. S. Dupuy, Variational projector augmented-wave method, *Comptes Rendus Mathematique*, 2017, **355**(6), 665–670.

78 A. Togo, F. Oba and I. Tanaka, First-principles calculations of the ferroelastic transition between rutile-type and $CaCl_2$-type SiO_2 at high pressures, *Phys. Rev. B: Condens. Matter Mater. Phys.*, 2008, **78**(13), 134106.

79 X. D. Wang, D. S. Wang, R. Q. Wu and A. J. Freeman, Validity of the force theorem for magnetocrystalline anisotropy, *J. Magn. Magn. Mater.*, 1996, **159**, 337–341.

80 J. Enkovaara and A. Ayuela, Magnetic anisotropy in Ni_2MnGa, *Phys. Rev. B: Condens. Matter Mater. Phys.*, 2002, **65**, 134422.

81 B. S. Yang, J. Zhang, L. N. Jiang, W. Z. Chen, P. Tang, X. G. Zhang, Y. Yan and X. F. Han, Strain induced enhancement of perpendicular magnetic anisotropy in Co/graphene and Co/BN heterostructures, *Phys. Rev. B*, 2017, **95**(17), 174424.

82 A. Hallal, H. X. Yang, B. Dieny and M. Chshiev, Anatomy of perpendicular magnetic anisotropy in Fe/MgO magnetic tunnel junctions: first-principles insight, *Phys. Rev. B: Condens. Matter Mater. Phys.*, 2013, **88**(18), 184423.

83 D. Z. Li, C. Barreteau, M. R. Castell, F. Silly and A. Smogunov, Out-*versus* in-plane magnetic anisotropy of free Fe and Co nanocrystals: tight-binding and first-principles studies, *Phys. Rev. B: Condens. Matter Mater. Phys.*, 2014, **90**(20), 205409.

84 X. D. Xu, Z. X. Chen, Y. Sakuraba, A. Perumal, K. Masuda, L. S. R. Kumara, H. Tajiri, T. Nakatani, J. Wang, W. Zhou, Y. Miura, T. Ohkubo and K. Hono, Microstructure, magnetic and transport properties of a Mn_2CoAl Heusler compound, *Acta Mater.*, 2019, **176**, 33–42.

85 X. R. Chen, M. M. Zhong, Y. Feng, Y. Zhou, H. K. Yuan and H. Chen, Structural, electronic, elastic, and thermodynamic properties of the spin-gapless semiconducting Mn_2CoAl inverse Heusler alloy under pressure, *Phys. Status Solidi B*, 2015, **252**(12), 2830–2839.

86 T. Zhou, Y. Feng, X. Chen, H. Yuan and H. Chen, Half-metallicity and magnetism of $Ti_2Ni_{1-x}Co_xAl_{1-y}Si_y$ inverse Heusler alloys, *J. Magn. Magn. Mater.*, 2017, **423**, 306–313.

87 T. Yang, L. Y. Hao, R. Khenata and X. T. Wang, Investigation of the structural competing and atomic ordering in Heusler compounds Fe_2NiSi and Ni_2FeSi under strain condition, *R. Soc. Open Sci.*, 2019, **6**(9), 191007.

88 J. Zhou, B. S. Sa, Z. M. Sun, C. Si and R. Ahujia, Manipulating carriers' spin polarization in the Heusler alloy Mn_2CoAl, *RSC Adv.*, 2015, **5**(90), 73814–73819.

89 P. V. Ong, N. Kioussis, P. K. Amiri, J. G. Alzate, K. L. Wang, G. P. Carman, J. Hu and R. Q. Wu, Electric field control and effect of Pd capping on magnetocrystalline anisotropy

in FePd thin films: a first-principles study, *Phys. Rev. B: Condens. Matter Mater. Phys.*, 2014, **89**(9), 094422.

90 D. Fritsch and C. Ederer, Epitaxial strain effects in the spinel ferrites $CoFe_2O_4$ and $NiFe_2O_4$ from first principles, *Phys. Rev. B: Condens. Matter Mater. Phys.*, 2010, **82**(10), 104117.

91 J. A. Heuver, A. Scaramucci, Y. Blickenstorfer, S. Matzen, N. A. Spaldin, C. Ederer and B. Noheda, Strain-induced magnetic anisotropy in epitaxial thin films of the spinel $CoCr_2O_4$, *Phys. Rev. B: Condens. Matter Mater. Phys.*, 2015, **92**(21), 214429.